The Astrophysical Journal Letters, 849:L6 (6pp), 2017 November 1 https://doi.org/10.3847/2041-8213/aa89e8

Halo Pressure Profile through the Skew Cross-power Spectrum of the Sunyaev–Zel'dovich Effect and CMB Lensing in *Planck*

Nicholas Timmons[1], Asantha Cooray[1], Chang Feng[1], and Brian Keating[2]
[1] Department of Physics and Astronomy, University of California, Irvine, CA 92697, USA
[2] Department of Physics, University of California, San Diego, La Jolla, CA 92093, USA
Received 2017 June 29; revised 2017 August 28; accepted 2017 September 1; published 2017 October 20

Abstract

We measure the cosmic microwave background (CMB) skewness power spectrum in *Planck*, using frequency maps of the HFI instrument and the Sunyaev–Zel'dovich (SZ) component map. The two-to-one skewness power spectrum measures the cross-correlation between CMB lensing and the thermal SZ effect. We also directly measure the same cross-correlation using the *Planck* CMB lensing map and the SZ map and compare it to the cross-correlation derived from the skewness power spectrum. We model fit the SZ power spectrum and CMB lensing–SZ cross-power spectrum via the skewness power spectrum to constrain the gas pressure profile of dark matter halos. The gas pressure profile is compared to existing measurements in the literature including a direct estimate based on the stacking of SZ clusters in *Planck*.

Key words: cosmology: observations

1. Introduction

The importance of the *Planck* mission (Planck Collaboration et al. 2011) to cosmology cannot be overstated. The measurement of cosmic microwave background (CMB) anisotropies has allowed for increased accuracy in measurements of cosmological parameters. Going beyond primary anisotropies *Planck* frequency maps can be used to probe higher-order correlations that arise from secondary effects like the Sunyaev–Zel'dovich (SZ) effect (Sunyaev & Zeldovich 1980), integrated Sachs–Wolfe (ISW) effect (Sachs & Wolfe 1967), and gravitational lensing (Smith et al. 2007), among others.

The SZ effect is the result of inverse Compton scattering of photons off free electrons. The SZ effect on the CMB is proportional to the integrated electron pressure inside galaxy clusters. Measurement of the SZ effect is a key tracer of the hot electron gas in the intracluster medium (ICM). Due to its unique frequency spectrum relative to the CMB blackbody, the thermal SZ effect can be separated in multi-frequency CMB maps (Cooray et al. 2000). Gravitational lensing of the CMB is caused by the intervening mass distribution and is a tracer of the line-of-sight projected matter potential. The integrated lensing map can be extracted from quadratic (Okamoto & Hu 2003) and likelihood (Hirata et al. 2008) estimators on CMB. A non-zero correlation between the lensing effect and the SZ effect establishes the relationship between dark matter and hot intracluster gas (Hill & Spergel 2014). This is an excellent probe of the large-scale distribution of gas. Several studies have attempted to look at this correlation (Cooray et al. 2000; Hill & Spergel 2014), including one using the *WMAP* data (Calabrese et al. 2010). Here, we update the previous work by incorporating data from *Planck*.

The cross-correlation between CMB lensing and thermal SZ results in a non-Gaussian signal at the three-point level of the correlation function (Spergel & Goldberg 1999; Cooray et al. 2000). While challenging to measure directly the bispectrum can be collapsed into a sum of two-point functions in what is known as the skewness power spectrum involving a squared temperature–temperature correlation. As has been shown in previous work (Cooray 2001; Munshi et al. 2011), the skewness spectrum, related to the CMB–CMB lensing–SZ bispectrum, can be probed through the cross-correlation of a temperature squared map and a map of the SZ effect. This skewness spectrum contains all the information from the bispectrum once the estimator is appropriately weighted. The three-point correlation function using only the CMB is an independent look at the lensing–SZ cross-correlation.

The amplitude of the non-Gaussian signals arising from the SZ effect can help constrain physical properties of the large-scale structure of the universe. Specifically, we consider here the gas pressure profile within galaxy clusters as a function of radius from the dark matter halo. Having a three-point correlation between the lensing and SZ effect can constrain parameters in the pressure profile model to reveal new physics regarding the relationship between dark matter and gas pressure.

The gas pressure profile of the ICM can be derived from the Navarro–Frenk–White profile assuming hydrostatic equilibrium (Navarro et al. 1996; Komatsu & Seljak 2001). Such a profile for the gas takes the form

$$\tilde{P}(x) = \frac{P_0}{(c_{500}x)^{\gamma}[1 + (c_{500}x)^{\alpha}]^{(\beta-\gamma)/\alpha}}. \quad (1)$$

The gas pressure profile is fully determined by the parameter set $\{P_0, c_{500}, \alpha, \beta, \gamma\}$, which are the central pressure, concentration, central slope, intermediate slope, and outer slope of the ICM pressure, respectively (Nagai et al. 2007). The gas pressure profile of galaxy clusters and its relation to the SZ effect has been studied by several groups, including Arnaud et al. (2010) and Planck Collaboration et al. (2013). In Planck Collaboration et al. (2013), the reconstructed SZ map was used to study the pressure of 62 massive clusters. By stacking radial profiles, the gas pressure profile was measured and the best-fit parameters were found to be $[P_0, c_{500}, \alpha, \beta, \gamma] = [6.41, 1.81, 1.33, 4.13, 0.31]$. It was

found that at large radii the pressure profile was flatter than simulations would predict. In Arnaud et al. (2010), simulations and observations of 33 clusters from *XMM-Newton* are used to create a profile for gas pressure and the resulting parameters are $[P_0, c_{500}, \alpha, \beta, \gamma] = [8.40, 1.18, 1.05, 5.49, 0.308]$. Recent work by Sayers et al. (2013) concluded that higher mass and larger redshift did not significantly affect the pressure profile. Sayers et al. (2013) used 45 massive galaxy clusters at $0.15 < z < 0.88$ and found the pressure profile parameters to be $[P_0, c_{500}, \alpha, \beta, \gamma] = [4.29, 1.18, 0.86, 3.67, 0.67]$. The CMB bispectrum measurement can be a complementary way to constrain the gas pressure parameters and provide additional observational evidence for probing the gas pressure profile.

The Letter is organized as follows: in the next section, we discuss the skewness estimator and its derivation. In Section 3, we review the data analysis preformed. In Section 4, the results of the analysis are presented. In Section 5, the Monte Carlo Markov Chain (MCMC) analysis is discussed along with the results and their cosmological implications. Section 6 is a summary of the findings and suggestions for future work. Throughout, we make use of the standard flat-ΛCDM cosmological model with $H_0 = 70$ km s^{-1} Mpc^{-1} and $\Omega_\Lambda = 0.73$.

2. Estimator

The derivation of the bispectrum and the skewness spectrum are discussed at length in several papers, including Cooray (2001) and more recently Munshi et al. (2011). Here, the authors cover the key points for this analysis and refer the reader to the previous work for a more detailed discussion. The angular bispectrum $B^{TTy}_{\ell_1\ell_2\ell_3}$ is defined as a triangle with sides (ℓ_1, ℓ_2, ℓ_3) in multipole space where $T(\boldsymbol{n})T(\boldsymbol{n})$ and $y(\boldsymbol{n})$ are statistically isotropic fields, with T representing a temperature map and y representing the SZ y-component map. The bispectrum is related to the multipole moments of the fields by

$$B^{TTy}_{\ell_1\ell_2\ell_3} = \sum_{m_1 m_2 m_3} \begin{pmatrix} \ell_1 & \ell_2 & \ell_3 \\ m_1 & m_2 & m_2 \end{pmatrix} \langle a^T_{\ell_1 m_1} a^T_{\ell_2 m_2} a^y_{\ell_3 m_3} \rangle. \quad (2)$$

The skewness power spectrum is the correlation of the product maps $T(\boldsymbol{n})T(\boldsymbol{n})$ and $y(\boldsymbol{n})$. This is useful because the angular bispectrum $B^{TTy}_{\ell_1\ell_2\ell_3}$ can be difficult to measure fully. The skewness spectrum $C_\ell^{TT,y}$ is a summation of the triangular configurations keeping one of the sides length ℓ fixed. Following the discussion in Cooray (2001), Calabrese et al. (2010), and Munshi et al. (2011), the bispectrum can be described by

$$B^{TTy}_{\ell_1\ell_2\ell_3} = -\Bigg[C^{\phi y}_{\ell_1} C_{\ell_1} \frac{\ell_2(\ell_2+1) - \ell_1(\ell_1+1) - \ell_3(\ell_3+1)}{2} + \text{perms.} \Bigg] \sqrt{\frac{(2\ell_1+1)(2\ell_2+1)(2\ell_3+1)}{4\pi}} \begin{pmatrix} \ell_1 & \ell_2 & \ell_3 \\ 0 & 0 & 0 \end{pmatrix}. \quad (3)$$

Here, $C_\ell^{\phi y}$ is the amplitude of the cross-correlation power spectrum between the lensing potential and the y-parameter map, and C_{ℓ_i} is the unlensed CMB anisotropy power spectrum. Only the permutations in which ℓ_1 and ℓ_2 vary are used since ℓ_3 remains tied to the secondary anisotropy and is fixed to relate to the skewness spectrum.

From Calabrese et al. (2010) and Munshi et al. (2011) the optimized skewness estimator begins with defining a set of nine weighted temperature maps:

$$\begin{aligned} X^1_{\ell m} &= \frac{a_{\ell m}}{\tilde{C}_\ell} C_\ell;\ Y^1_{\ell m} = \ell(\ell+1)\frac{a_{\ell m}}{\tilde{C}_\ell};\ Z^1_{\ell m} = \frac{a_{\ell m}}{\tilde{C}_\ell} C^{\phi y}_\ell \\ X^2_{\ell m} &= -\ell(\ell+1)\frac{a_{\ell m}}{\tilde{C}_\ell} C_\ell;\ Y^2_{\ell m} = \frac{a_{\ell m}}{\tilde{C}_\ell};\ Z^2_{\ell m} = \frac{a_{\ell m}}{\tilde{C}_\ell} C^{\phi y}_\ell \\ X^3_{\ell m} &= \frac{a_{\ell m}}{\tilde{C}_\ell} C_\ell;\ Y^3_{\ell m} = \frac{a_{\ell m}}{\tilde{C}_\ell};\ Z^3_{\ell m} = -\ell(\ell+1)\frac{a_{\ell m}}{\tilde{C}_\ell} C^{\phi y}_\ell, \end{aligned} \quad (4)$$

where $\tilde{C}_\ell = C_\ell + N_\ell / b_\ell^2$ is the temperature power spectrum, b_ℓ is the beam transfer function, and N_ℓ is the noise power spectrum. The nine weighted maps are generated by $T^{(i)}(\boldsymbol{n}) = \sum Y_{\ell m}(\boldsymbol{n}) T^{(i)}_{\ell m}$, where i is the index of the weighted map from above. The optimized skew spectrum is defined as

$$C_\ell^{XY,Z} = \frac{1}{2\ell+1} \sum_i \sum_m \text{Real}[(X^{(i)}(\boldsymbol{n}) Y^{(i)}(\boldsymbol{n}))_{\ell m} Z^{(i)}(\boldsymbol{n})_{\ell m}]. \quad (5)$$

The measured skewness spectrum $\hat{C}_\ell^{TT,y}$ now can be related to the bispectrum as shown in Cooray (2001), Munshi et al. (2011) as

$$\hat{C}_\ell^{XY,Z} = \frac{1}{2\ell+1} \sum_{\ell_1 \ell_2} \frac{\hat{B}_{\ell\ell_1\ell_2} B_{\ell\ell_1\ell_2}}{\tilde{C}_\ell \tilde{C}_{\ell_1} \tilde{C}_{\ell_2}}. \quad (6)$$

Here, $\hat{B}_{\ell\ell_1\ell_2}$ is the reduced bispectrum, meaning it has been weighted as the maps have in the derivation of $C_\ell^{TT,y}$, and the calculation only includes the permutations in which ℓ_3 is fixed. The range of ℓ is $2 < \ell < 1600$.

Now the measured skewness spectrum $\hat{C}_\ell^{TT,y}$ can be related to the theoretical $C_\ell^{TT,y}$. The theory $C_\ell^{TT,y}$ is calculated analytically by plugging the bispectrum formulation in Equation (2) into Equation (5). Up to this point the amplitude of the lensing–SZ cross-correlation $C_\ell^{\phi y}$ has been taken to be unity. While the measured spectrum contains one factor of $C_\ell^{\phi y}$ and one factor of $\hat{C}_\ell^{\phi y}$, the theory spectrum contains two factors of $C_\ell^{\phi y}$. The ratio of the measured and theoretical spectra gives the measured lensing–SZ cross-correlation $\hat{C}_\ell^{\phi y}$.

3. Data Analysis

For the purposes of this analysis the *Planck* PR2-2015 all-sky maps were used. Specifically, the 100 GHz, 143G Hz, and 217 GHz temperature maps were used, as was the MILCA full mission y-map component foreground map. The data were reduced using custom python scripts within the HEALPY[3] (Górski et al. 2005) code framework. Briefly, the temperature maps were masked using a combination of Galactic foreground mask and the *Planck*-released point-source map. The 60% foreground mask in conjunction with a point-source mask was utilized in order to mask out any contamination by the Milky Way galaxy and bright sources. The monopole signal as well as the dipole signal were modeled using HEALPY and removed before measuring the power spectrum.

In order to measure the noise N_ℓ for the temperature maps, 100 *Planck*-released simulated noise maps were passed through the analysis pipeline, and the resulting median power spectrum was determined to be the noise contribution to the measured power spectrum. The CMB anisotropy power spectrum C_ℓ was

[3] http://healpix.sourceforge.net

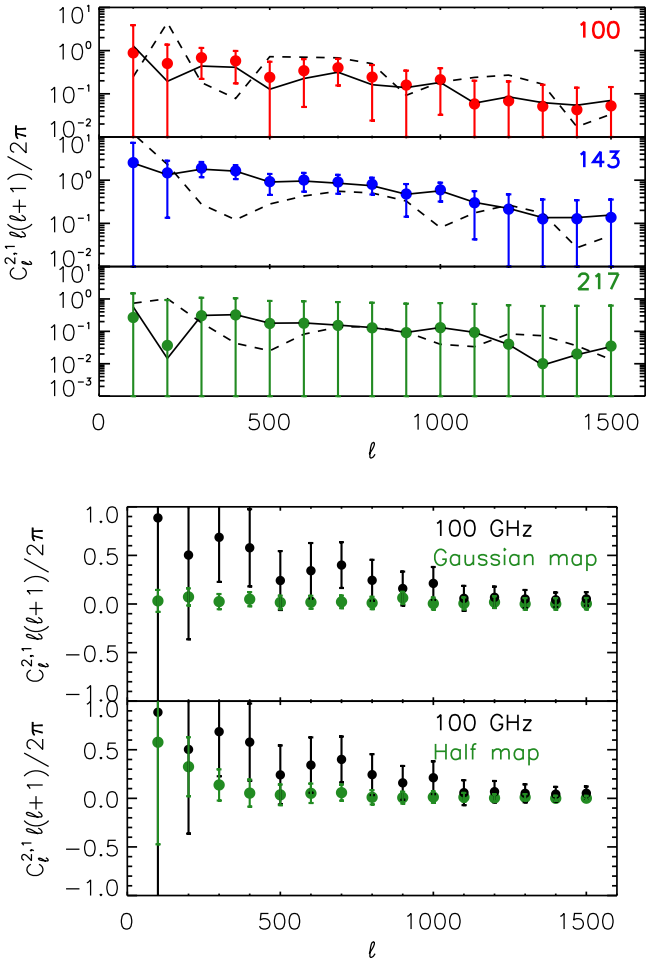

Figure 1. Top: the measured skewness spectrum for each of the three frequencies. From top to bottom, 100 GHz, 143 GHz, and 217 GHz, respectively. The contributions of the dust signal and the SZ signal in the temperature maps are plotted as well. The dashed line is the resulting spectrum after subtracting the *Planck* dust map from the *y*-parameter map. The solid line is the resulting spectrum after having subtracted the frequency-corrected *y*-map from the temperature map. Bottom: the result of passing a Gaussian map with noise through the estimator and the result of passing the half-map difference through the estimator. For comparison, the 100 GHz skewness spectrum is plotted. Both results are consistent with a null result as would be expected.

generated using the CAMB (Lewis 2013) code, the result of which was in agreement with the measured CMB power spectrum released by the *Planck* team. To model the noise in the *y*-map, the *Planck*-released MILCA homogeneous noise power spectrum was used.

To measure the direct cross-correlation between lensing and tSZ (Spergel & Goldberg 1999), the *Planck*-released lensing map was similarly masked before being cross correlated with the component *y*-map to measure $C_\ell^{\phi y}$. To measure the dust contamination, the *Planck*-released dust map was used and subtracted from the temperature maps before being run through the data pipeline.

4. Results

In the top portion of Figure 1, we show the resulting skewness power spectra from the different frequencies with error bars from the simulated noise maps as well as cosmic variance. While there is a similar signal in the 100 and 143 GHz spectra the 217 GHz spectrum shows a deficiency. This is due to the SZ effect being frequency dependent with a smaller signal at 217 GHz compared to 100 and 143 GHz. Also plotted are the contribution of the dust and SZ effect on the temperature maps. The dashed line represents the skewness power spectra when the *Planck* dust map is subtracted from the *y*-parameter map before being correlated with the temperature squared map. From the results it does not appear that the dust contribution to the *y*-parameter map is significant. The solid line represents subtracting a scaled *y*-parameter map from the temperature maps before squaring them and correlating with the *y*-parameter map. The solid line shows that the SZ signal does not contaminate the temperature maps.

Subtracting the dust map from the *y*-parameter map is a test for the cosmic infrared background (CIB) contamination in the *y*-map as dust is a tracer of the CIB. While the subtracted dust map skewness spectra do not show a statistically significant difference from the non-subtracted spectra it is worth noting that removing the CIB leakage from the *y*-map is a difficult task and has been the subject of analysis in several articles (Hill & Spergel 2014; Planck Collaboration et al. 2016b). In Planck Collaboration et al. (2016a), the correlation between the SZ effect and the CIB is measured. From those results, the CIB contamination contributes as much as 20% of the signal at intermediate and small angular scales.

The results of the data pipeline null test are shown in the bottom panels of Figure 1. The upper panels shows the result when passing a simple Gaussian map with simulated noise through the pipeline. The bottom panels show the result when using a map made up of the difference between two half-maps. For comparison, the 100 GHz spectrum is plotted. If there is no systematic contribution to the signal in the data pipeline, both the Gaussian and half-map spectra should be consistent with zero. While the error is large in the half-map spectrum, both results show that the signal in the 100 GHz spectrum is not coming from systematics and is non-vanishing.

The contributions from various error estimates are plotted in the top panel of Figure 2. In the figure, the 100 GHz skewness spectrum is plotted and is representative of the other frequencies. To estimate the error contribution from the temperature maps, 100 *Planck* simulated noise maps at each frequency were passed through the data pipeline. The standard deviation of the resulting power spectra became the error estimate. The dominate source of error is from the simulated temperature noise maps, while the noise contribution from the *y*-parameter map is not as significant. The contribution from cosmic variance is not significant. At high ℓ all of the noise contributions become significant with the temperature map noise rising above the signal. The bottom panel of Figure 2 contains a histogram plot of the skew spectrum value at $\ell = 1000$ for the 100 GHz simulated noise maps shown. The noise contribution is almost Gaussian as expected over 100 simulated maps.

5. MCMC and Model Interpretation

Figure 3 shows the measured three-point lensing convergence–SZ cross-correlation power spectrum $C_\ell^{\kappa y}$ and the measured two-point *y*-parameter auto-power spectrum C_ℓ^{yy}. From the MCMC procedure, we obtain the best-fit models for each case and have plotted the result. The measured lensing–SZ cross-correlation comes from the resulting skewness power spectra that has been averaged over the three frequency bands

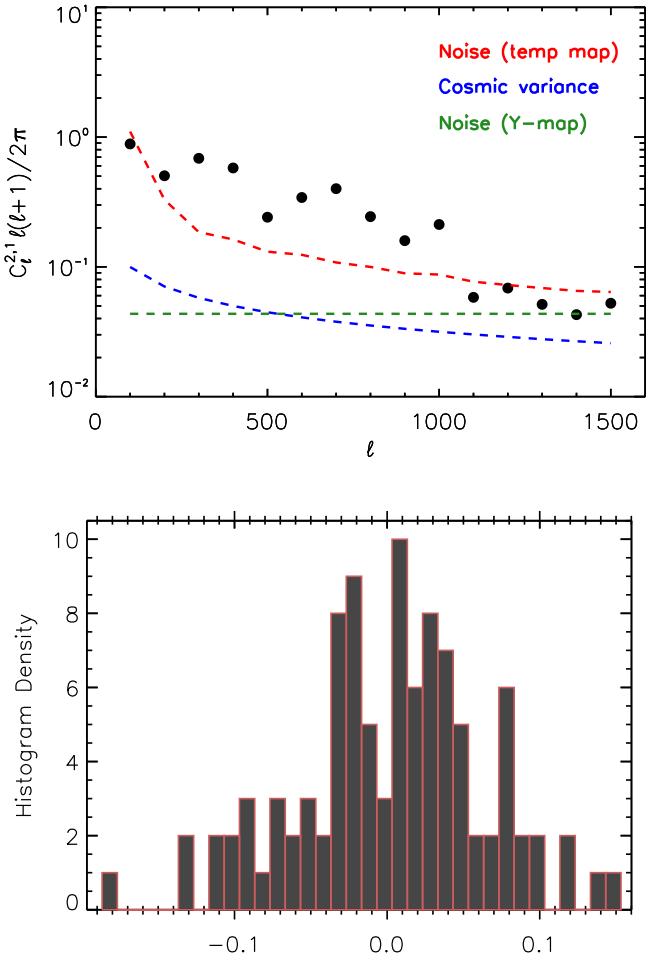

Figure 2. Top: the component contributions to the total error. The 100 GHz spectrum is shown as an example that is representative of all three frequencies. Bottom: a histogram of the variance in the signal of the simulated noise. One hundred simulated maps were put through the same estimator as the data, and the value at $\ell = 1000$ is plotted here.

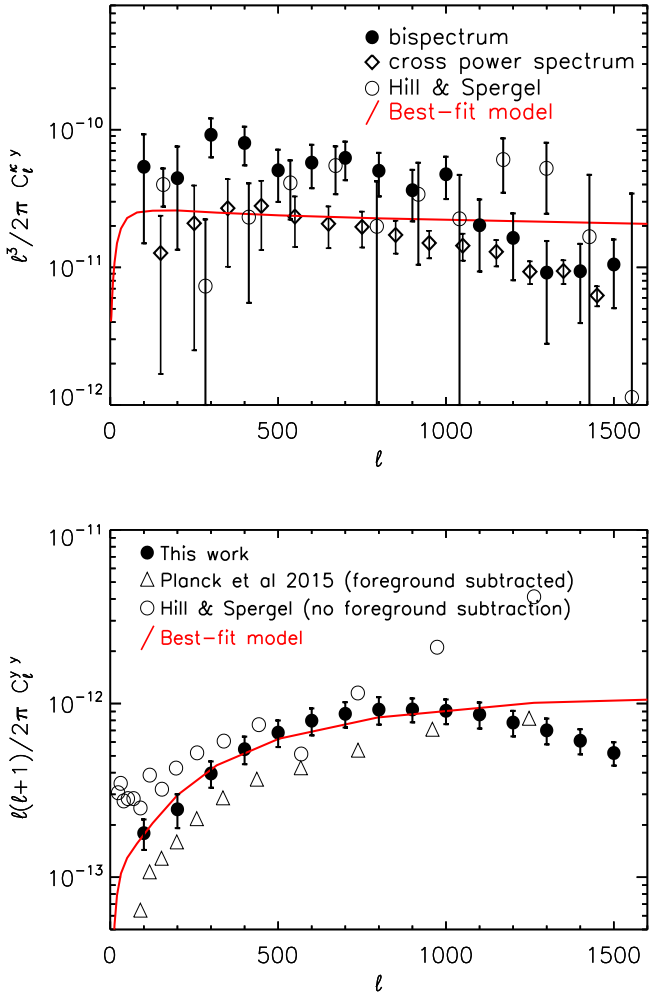

Figure 3. Best-fit models of the cross-power spectrum $C_\ell^{\kappa y}$ and auto-power spectrum C_ℓ^{yy} are plotted in red. They are compared to the measured cross-power spectrum from the skew spectrum analysis, the direct cross-power spectrum of the *Planck* lensing map with the *y*-parameter map, as well as the auto-power spectrum of the *Planck* *y*-parameter maps. The results from Hill & Spergel (2014), as well as Planck Collaboration et al. (2016b), are shown as a comparison, being the direct two-point lensing–SZ cross-correlation and the *y*-map auto-spectrum from the generated maps therein. The error bars for Planck Collaboration et al. (2016b) are smaller than the symbols used in the plot.

with error added in quadrature. Because of the noise dominance, the covariance in error between the three frequencies is not significant and is neglected. Also shown is the measured cross-correlation of the *Planck* lensing map with the *y*-parameter map as well as the two-point lensing–SZ cross-correlation measured in Hill & Spergel (2014). The two-point *y*-parameter auto-power spectrum is measured by taking the auto-spectrum of the *Planck* *y*-parameter map. For comparison the Hill & Spergel (2014) auto-spectrum is shown, as is the Planck Collaboration et al. (2016b) auto-spectrum. The spectrum from Hill & Spergel (2014) can be considered as a raw spectrum with no foreground subtraction, while the Planck Collaboration et al. (2016b) spectrum has had foreground contaminants removed. See Planck Collaboration et al. (2016b) for more details. At intermediate and small angular scales the raw spectrum includes contributions from the CIB, while the foreground subtracted spectrum does not.

The best-fit model for the gas pressure from the three-point correlation is shown in Figure 4 along with the 1σ confidence region. For comparison gas pressure profiles from *Planck* and *XMM-Newton* are shown (Arnaud et al. 2010; Planck Collaboration et al. 2013) as well as the higher-z clusters from Sayers et al. (2013).

We follow the gas pressure model in Arnaud et al. (2010), i.e.,

$$P_e(r) = 1.65 h_{70}^2 E^{8/3}(z)\left[\frac{M_{500}}{3\times 10^{14} M_\odot/h_{70}}\right]^{2/3+\alpha_P} \times \tilde{P}(x)(\mathrm{eV\ cm^{-3}}). \quad (7)$$

Here, $E(z) = H(z)/H_0$, $h_{70} = h/0.7$ and $\alpha_P = 0.12$. We determine the radius r_{500} from the relation $M_{500} = 4\pi/3[500\rho_c(z)]r_{500}^3$. In this equation, $\rho_c(z)$ is the critical density and $x = r/r_{500}$.

We use the halo model (Cooray & Sheth 2002) to predict the theoretical power spectra C_ℓ^{yy} and $C_\ell^{\kappa y}$ following the calculations of one-halo and two-halo terms (Hill & Spergel 2014; Planck Collaboration et al. 2014; Battaglia et al. 2015). The gas pressure profile in this work is taken from Arnaud et al. (2010) and Ma et al. (2015), where the parameter set is assumed to be independent of mass and redshift. However, in Battaglia et al. (2015), some of the parameters can vary with mass and redshift, and they verified that the halo model calculation was

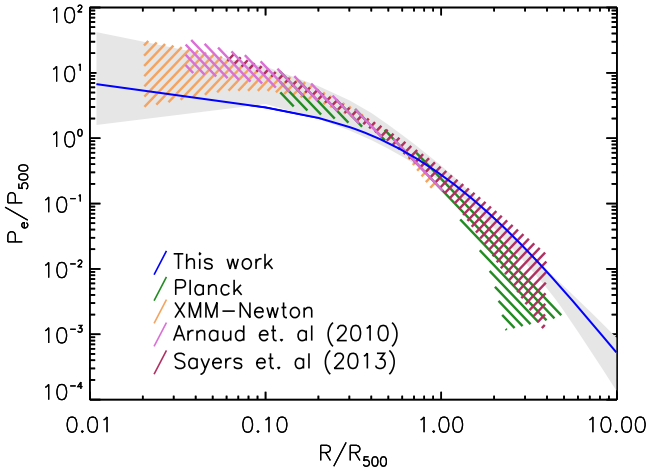

Figure 4. Best-fit model of the gas pressure $P_e(r)$ including the 1σ confidence region shown by the shaded region. For comparison the pressure profiles measured in Planck Collaboration et al. (2013), Arnaud et al. (2010), and Sayers et al. (2013) are also shown as a 1σ region. The pressure profiles have been set to $z = 0$ for comparison.

largely consistent with the measurements from numerical simulations. We do not expect significant differences between these gas pressure models, given the weak dependence on the mass and redshift and the limited constraining power of the measured cross-power spectrum. However, to produce the most precise gas pressure profile, one has to rely on numerical simulations. We compare the theoretical power spectra of both C_ℓ^{yy} and $C_\ell^{\kappa y}$ to the measured ones, sampling the gas pressure profiles and generating posterior distribution functions from the following likelihood:

$$-2\ln\mathcal{L} = \sum_{i=\kappa y,yy}\sum_b \left[\frac{C_b^{\mathrm{obs},(i)} - \hat{C}_b^{(i)}}{\Delta_b}\right]^2 + \text{const.} \qquad (8)$$

Such an MCMC procedure generates a sufficient amount of samples of the parameters for the gas pressure profile, among which we can obtain the best-fit model corresponding to the smallest chi-square. In Figure 3, we show the best-fit model for the Planck lensing and tSZ, while in Van Waerbeke et al. (2014) a similar analysis was performed with the shear measurements of the Canada–France–Hawaii Telescope Lensing Survey and a newly constructed tSZ map from Planck.

6. Discussion

As demonstrated, the three-point measurement from the skew spectrum is in agreement with the two-point direct measurement from Hill & Spergel (2014). It serves as an independent check on the work done before and can be used to constrain physical properties like the gas pressure profile. The non-zero result confirms the correlation between dark matter CMB lensing and the hot ICM traced by the thermal SZ effect.

Using only the CMB, the gas pressure profile is examined as a separate check on the work done by observing clusters directly or by simulation. The resulting gas pressure profiles from the MCMC procedure defined by the parameters $\{P_0, c_{500}, \alpha, \beta, \gamma\}$ are $\{5.1^{+2.0}_{-1.8}, 1.7^{+0.6}_{-0.5}, 1.2^{+0.5}_{-0.3}, 3.2^{+0.4}_{-0.3}, 0.3^{+0.2}_{-0.1}\}$. These parameters are in agreement with the literature in which observations and simulations are conducted to measure the profile.

It should be noted that Planck Collaboration et al. (2013), Arnaud et al. (2010), and Sayers et al. (2013) are probing high-mass clusters while the cross-spectrum is more sensitive to the lower-mass clusters (Battaglia et al. 2015). While Sayers et al. (2013) found that the gas pressure profile is nearly universal over a wide range of masses/redshifts, simulations have shown that the profile can be sensitive to these parameters (Le Brun et al. 2015).

As can be seen in Figure 4, the pressure profile from this work is in agreement with the work done by observations from *Planck*, *XMM-Newton*, and *Chandra*, as well as simulations. Considering the differences in mass between this work and the observational/simulation work in the literature, the gas pressure profiles are of a similar shape within 1σ. This would lend credence to the idea that the gas pressure profile is more universal over a wide range of masses/redshifts. As a check the two-point correlation was also modeled for the pressure profile and found to not vary significantly from the three-point model.

7. Summary

The CMB skewness power spectrum was measured using the correlation between *Planck* frequency maps and *Planck* SZ component maps. We also measure the lensing–thermal SZ cross-correlation power spectrum using the three-point correlation function (bispectrum) and compare it to the two-point correlation direct measurements from *Planck* all-sky maps.

The MCMC procedure is utilized in order to find the best-fit lensing cross-correlation power spectrum as well as the best-fit y-parameter auto-spectrum. The best-fit and uncertainty values for the gas pressure parameters found to be $\{P_0, c_{500}, \alpha, \beta, \gamma\}$ are $\{5.1^{+2.0}_{-1.8}, 1.7^{+0.6}_{-0.5}, 1.2^{+0.5}_{-0.3}, 3.2^{+0.4}_{-0.3}, 0.3^{+0.2}_{-0.1}\}$, where P_0, c_{500}, α, β, and γ are the central pressure, concentration, central slope, intermediate slope, and outer slope, respectively. The parameters are found to be in agreement with the literature.

N.T., C.F., and A.C. would like to acknowledge support from NASA grants NASA NNX16AJ69G and NASA NNX16AF39G, *HST*-AR-13886.001-A, IGPP LANL 368641, NSF AST-1313319, and Ax Foundation for Cosmology at UC San Diego. Some of the results in this Letter have been derived using the HEALPix (Górski et al. 2005) package.

ORCID iDs

Nicholas Timmons https://orcid.org/0000-0001-6471-4625

References

Arnaud, M., Pratt, G. W., Piffaretti, R., et al. 2010, A&A, 517, A92
Battaglia, N., Hill, J. C., & Murray, N. 2015, ApJ, 812, 154
Calabrese, E., Smidt, J., Amblard, A., et al. 2010, PhRvD, 81, 043529
Cooray, A. 2001, PhRvD, 64, 043516
Cooray, A., Hu, W., & Tegmark, M. 2000, ApJ, 540, 1
Cooray, A., & Sheth, R. 2002, PhR, 372, 1
Górski, K. M., Hivon, E., Banday, A. J., et al. 2005, ApJ, 622, 759
Hill, J. C., & Spergel, D. N. 2014, JCAP, 2, 030
Hirata, C. M., Ho, S., Padmanabhan, N., Seljak, U., & Bahcall, N. A. 2008, PhRvD, 78, 043520
Komatsu, E., & Seljak, U. 2001, MNRAS, 327, 1353
Le Brun, A. M. C., McCarthy, I. G., & Melin, J.-B. 2015, MNRAS, 451, 3868
Lewis, A. 2013, PhRvD, 87, 103529
Ma, Y.-Z., Van Waerbeke, L., Hinshaw, G., et al. 2015, JCAP, 9, 046
Munshi, D., Heavens, A., Cooray, A., & Valageas, P. 2011, MNRAS, 414, 3173
Nagai, D., Kravtsov, A. V., & Vikhlinin, A. 2007, ApJ, 668, 1
Navarro, J. F., Frenk, C. S., & White, S. D. M. 1996, ApJ, 462, 563

Okamoto, T., & Hu, W. 2003, PhRvD, 67, 083002
Planck Collaboration, Ade, P. A. R., Aghanim, N., et al. 2011, A&A, 536, A1
Planck Collaboration, Ade, P. A. R., Aghanim, N., et al. 2013, A&A, 550, A131
Planck Collaboration, Ade, P. A. R., Aghanim, N., et al. 2014, A&A, 571, A21
Planck Collaboration, Ade, P. A. R., Aghanim, N., et al. 2016a, A&A, 594, A23
Planck Collaboration, Aghanim, N., Arnaud, M., et al. 2016b, A&A, 594, A22
Sachs, R. K., & Wolfe, A. M. 1967, ApJ, 147, 73
Sayers, J., Czakon, N. G., Mantz, A., et al. 2013, ApJ, 768, 177
Smith, K. M., Zahn, O., & Doré, O. 2007, PhRvD, 76, 043510
Spergel, D. N., & Goldberg, D. M. 1999, PhRvD, 59, 103001
Sunyaev, R. A., & Zeldovich, I. B. 1980, MNRAS, 190, 413
Van Waerbeke, L., Hinshaw, G., & Murray, N. 2014, PhRvD, 89, 023508